

1 **Vermiculite as heterogeneous catalyst in electrochemical Fenton-**
2 **based processes: Application to the oxidation of Ponceau SS dye**

3 Aleksandro Jhones dos Santos^a, Ignasi Sirés^a, Ana P.M. Alves^b, Carlos A. Martínez-
4 Huitle^c, Enric Brillas^{a,*}

5 ^a *Laboratori d'Electroquímica dels Materials i del Medi Ambient, Departament de Química Física,*
6 *Facultat de Química, Universitat de Barcelona, Martí i Franquès 1-11, 08028 Barcelona, Spain*

7 ^b *Departamento de Química, Universidade Federal da Paraíba, João Pessoa - CEP 58.051-900,*
8 *PB, Brazil*

9 ^c *Laboratório de Eletroquímica Ambiental e Aplicada, Instituto de Química, Universidade Federal*
10 *do Rio Grande do Norte, Lagoa Nova - CEP 59.072-900, Natal, RN, Brazil*

11 *Corresponding author: *E-mail address:* brillas@ub.edu (E. Brillas)

12

13 **Abstract**

14 Modified sodium vermiculite, an iron-rich clay mineral, has been used in novel heterogeneous
15 electrochemical Fenton-based treatments, so-called electro-Fenton (EF)-vermiculite, UVA
16 photoelectro-Fenton (PEF)-vermiculite and solar photoelectro-Fenton (SPEF)-vermiculite. Tests
17 were made with 130 mL of 0.150 mM Ponceau SS diazo dye in 0.050 M Na₂SO₄ at pH 3.0, in the
18 presence of 1.0 g L⁻¹ catalyst microparticles. The electrolyses were performed in an undivided cell
19 with a boron-doped diamond anode (BDD) and air-diffusion cathode for H₂O₂ production, at 33.3
20 mA cm⁻². Decolorization and mineralization were upgraded in the sequence: EF-vermiculite <
21 PEF-vermiculite < SPEF-vermiculite. The removal of organics occurred by the combined action
22 of •OH oxidant formed at the BDD surface and homogeneous and heterogeneous Fenton's
23 reactions, along with the photolysis caused by UVA light or sunlight. The homogeneous Fenton's
24 reaction resulted from iron ions leaching, but the heterogeneous mechanism was prevalent.
25 Comparative treatments by anodic oxidation in the presence of H₂O₂ and homogeneous EF were
26 less effective than EF-vermiculite. The diazo dye absorbance decays agreed with a pseudo-first-
27 order kinetics. SPEF-vermiculite was the most powerful process, yielding total decolorization and
28 84.1% mineralization after 300 and 360 min, respectively. The influence of catalyst concentration,
29 current density and diazo dye content on PEF-vermiculite performance was examined. Oxalic,
30 oxamic, malic, tartronic and acetic acids were detected as final short-linear carboxylic acids.

31 *Keywords:* Heterogeneous electro-Fenton; Heterogeneous Fenton; Mineral catalyst;
32 Heterogeneous photoelectro-Fenton; Ponceau SS; Water treatment

33 1. Introduction

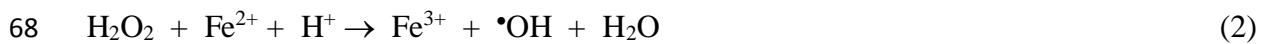
34 The high effectiveness of the electrochemical advanced oxidation processes (EAOPs) for the
35 destruction of refractory organic pollutants in synthetic and real wastewater has been recently
36 reported (Panizza and Cerisola, 2009; Oturan and Aaron, 2014; Sirés et al., 2014; Brillas and
37 Martínez-Huitle, 2015; Martínez-Huitle et al., 2015). These environmentally friendly methods
38 produce a large amount of homogeneous or heterogeneous hydroxyl radicals ($\cdot\text{OH}$), strong
39 oxidants ($E^\circ = 2.80 \text{ V/SHE}$ at pH 0) that can attack repeatedly the organics causing their
40 mineralization. In anodic oxidation (AO), a high current supply allows the formation of
41 heterogeneous radicals ($\text{M}(\cdot\text{OH})$) at the anode surface (M) as intermediate of O_2 discharge,
42 according to water oxidation reaction (1) (Boye et al., 2002; Santos et al., 2008; Panizza and
43 Cerisola, 2009). Non-active boron-doped diamond (BDD) anodes are preferred in AO because
44 they produce large quantities of BDD($\cdot\text{OH}$) (Polcaro et al., 2003; Mascia et al., 2011; Bezerra
45 Rocha et al., 2012; Lanzalaco et al., 2018).



47 In a one-compartment cell, the oxidation ability of AO can be enhanced if a weaker oxidant
48 such as H_2O_2 is continuously generated at a carbonaceous cathode from the two-electron reduction
49 of injected O_2 , giving rise to the AO- H_2O_2 process (Brillas et al., 2009). Carbon felt (Panizza et
50 al., 2014; Dominguez et al., 2018; Ganzenko et al., 2018), reticulated vitreous carbon (Coria et al.,
51 2015; Ellouze et al., 2017) and carbon-polytetrafluoroethylene (PTFE) air-diffusion (Olvera-
52 Vargas et al., 2015; Galia et al., 2016; dos Santos et al., 2018a, 2018b) materials have been
53 employed for an effective H_2O_2 generation.

54 The oxidation power of electrogenerated H_2O_2 is strongly enhanced in Fenton-based EAOPs
55 like electro-Fenton (EF), UVA photoelectro-Fenton (PEF) and solar photoelectro-Fenton (SPEF)
56 (Brillas et al., 2009; Salazar et al., 2011; Thiam et al., 2015; Lanzalaco et al., 2017; Flores et al.,

2018; Ye et al., 2019). These processes are typically applied under homogeneous conditions, with addition of soluble Fe²⁺ catalyst to the treated solution to form Fe³⁺ and homogeneous •OH via Fenton's reaction (2) at pH near 3.0 (Brillas et al. 2009; Sirés et al., 2014; Steter et al. 2018). Fe³⁺ may be an alternative iron source because it can be cathodically reduced to Fe²⁺, thus sustaining the Fenton's reaction. In EF, the BDD anode confers superior oxidation ability thanks to the combination of heterogeneous BDD(•OH) and homogeneous •OH (Coria et al., 2016; Steter et al., 2016). In contrast, the anode composition is less relevant in PEF and SPEF, since photons from UVA light and sunlight stimulate the production of homogeneous •OH from Fe(OH)²⁺ photolysis. In addition, they promote the photodecomposition of Fe(III) complexes of generated carboxylic acids, thus accelerating the mineralization of the target molecule (Salazar et al., 2012; Brillas, 2014; Pérez et al., 2017; Fajardo et al., 2019).



Lately, heterogeneous EAOPs like hetero-EF and hetero-PEF with solid mineral catalysts (goethite, magnetite or pyrite) or synthesized catalysts are being studied with particular interest (Ganiyu et al., 2018; Poza-Nogueiras et al., 2018). In these methods, the main degradation route of organics involves heterogeneous hydroxyl radicals formed from heterogeneous Fenton's reaction between Fe(II) and H₂O₂ at the catalyst surface, which allows extending the treatment to circumneutral pH conditions. Since most of these catalysts release iron ions to the solution, homogeneous and heterogeneous Fenton processes occur in practice. The search of insoluble and cheap materials is mandatory to further develop the heterogeneous EAOPs with minimization of iron sludge precipitation.

Natural and modified vermiculite clays are cheap layered materials. Vermiculite is widely available on the planet, being Brazil one of its larger producers. Its excellent thermal resistance, light weight and water-wicking ability constitute an advantage in many industrial and environmental applications (Ferma Group, 2019). Vermiculite belongs to the 2:1 group of hydrous

82 phyllosilicate minerals composed of hydrated silicates of magnesium, iron and aluminum
83 $[(\text{Mg,Fe})_3(\text{Si,Al})_4\text{O}_{10}][\text{OH}]_2 \cdot 4\text{H}_2\text{O}$) (Batista et al., 2019). Its structure consists of an octahedral
84 sheet of magnesia or alumina sandwiched between two tetrahedral silicate sheets, having a
85 negative charge that is balanced by interlamellar cations (Chen et al., 2010, Batista et al., 2019).
86 The high specific area and porosity of these minerals make them suitable candidates for oil
87 adsorption (Purceno et al., 2012) or pyrolysis (Batista et al., 2019). Vermiculite contains covalently
88 bound iron ions, with a typical surface distribution of about 20% Fe^{2+} and 80% Fe^{3+} (Purceno et
89 al. 2012). This has been utilized for the reduction of water contaminants like Cr(VI) (Liu et al.,
90 2011) and chlorinated ethylenes (Lee and Batchelor, 2004). Some authors have employed natural
91 and modified vermiculite particles as heterogeneous catalysts in Fenton (Purceno et al., 2012) and
92 photo-Fenton (Chen et al., 2010; Yang et al., 2018; Martínez-Costa et al., 2018, 2019). Table SM-
93 1 collects the main results obtained for different pollutants, evidencing the excellent catalytic
94 power of vermiculite in heterogeneous Fenton's reaction. Nonetheless, no previous studies report
95 its use in heterogeneous Fenton-based EAOPs. On the other hand, several clays like kaolinite can
96 adsorb organics to large extent and this allows their removal by electrokinetic treatment (Polcaro
97 et al., 2007).

98 A large plethora of aromatic azo dyes with one or various -N=N- bonds is produced annually
99 (Rajkumar and Kim, 2006). Since they present different colors as a function of the benzenic rings
100 involved, azo dyes are widely used in textile and food industries, resulting in highly contaminated
101 wastewater containing up to 250 mg L^{-1} of dyes (Zollinger, 2003; Solís et al., 2012; Brillas and
102 Martínez-Huitle, 2015). The aesthetic problems related to this kind of wastewater (dos Santos et
103 al., 2007; UNESCO, 2012), along with the great stability, toxicity, carcinogenicity and
104 mutagenicity of azo dyes and their by-products (Sharma et al., 2007; Ulson de Souza et al., 2007),
105 derive in an urgent necessity to upgrade their removal. Unlike conventional treatments such as
106 adsorption and coagulation (Bhattacharya and Sanghi, 2003; dos Santos et al., 2007; Verma et al.,

107 2012), oxidation with $\bullet\text{OH}$ generated in homogeneous and heterogeneous Fenton-based EAOPs is
108 quite effective to reach this purpose (Brillas and Martínez-Huitle, 2015; Hafaiedh et al., 2018).

109 The aim of this work is to investigate whether the novel EF-vermiculite, PEF-vermiculite and
110 SPEF-vermiculite processes, i.e., the EF, PEF and SPEF treatments run with vermiculite as
111 heterogeneous catalyst, are viable for the degradation of organic pollutants in water. Modified
112 sodium vermiculite was used because better catalytic properties are expected upon surface
113 replacement of alkaline earth metals by Na^+ (Batista et al., 2019). The performance of the
114 heterogeneous Fenton-based EAOPs was assessed from the decolorization and mineralization of
115 solutions of a commercial salt of Ponceau SS diazo dye (see its physicochemical characteristics in
116 Table SM-2). This compound was chosen because it can be effectively destroyed by EF and PEF
117 treatments at pH 3.0 using a BDD anode (dos Santos et al., 2018a). All the assays were made with
118 0.050 M Na_2SO_4 as supporting electrolyte. Comparative trials by AO- H_2O_2 and homogeneous EF
119 with soluble Fe^{2+} were carried out to clarify the homogeneous and heterogeneous reaction paths.
120 The effect of current density (j) and contents of catalyst and diazo dye on the decolorization and
121 mineralization rates in PEF-vermiculite was examined.

122 **2. Materials and methods**

123 *2.1. Chemicals*

124 Disodium Ponceau SS was purchased from Sigma-Aldrich and its purity (80%, the rest
125 corresponding to inorganic stabilizers) was confirmed by total organic carbon (TOC) analysis.
126 Standard carboxylic acids were of analytical grade purchased from Merck, Fluka and Panreac.
127 Solutions were prepared with high-purity water from a Millipore Milli-Q system, with resistivity
128 $> 18.2 \text{ M}\Omega \text{ cm}$ at ambient temperature. The solution pH was adjusted with analytical grade sulfuric
129 acid (96% purity) purchased from Acros Organics. Analytical grade sodium sulfate used as
130 background electrolyte was purchased from Prolabo. The catalyst used for homogeneous EF was

131 analytical grade heptahydrated Fe(II) sulfate purchased from Fluka. Other chemicals used for
132 analysis were of analytical or HPLC grade supplied by Panreac and Merck.

133 *2.2. Preparation of sodium vermiculite*

134 The raw vermiculite clay powder was obtained in the municipality of Santa Luzia (Paraíba,
135 Brazil). Aiming to improve its performance as heterogeneous catalyst, it was conditioned as
136 reported elsewhere (Batista et al., 2019). Briefly, a mass of 400 g of the raw material was washed
137 with distilled water and further, dried for 2 d at room temperature. It was then mixed with 250 mL
138 of acetate/acetic acid buffer solution at pH near 5 under vigorous stirring, and 250 mL of 30%
139 H₂O₂ were added to clean its surface. This suspension was maintained at 50 °C for 72 h and then,
140 the resulting powder was washed with distilled water and dried at 100 °C for 24 h. Finally, sodium
141 vermiculite was obtained by cationic exchange with 1 M NaCl.

142 *2.3. Electrochemical advanced oxidation treatments*

143 The electrolytic experiments were made in an open, undivided and cylindrical glass tank
144 reactor containing 130 mL of stirred solution. The solution temperature was maintained at 25 °C
145 by means of external thermostated water circulating through a jacket surrounding the cell. A thin-
146 layer of BDD on Si substrate purchased from NeoCoat was used as the anode. The cathode was a
147 carbon-PTFE air-diffusion electrode supplied by E-TEK, which was fed with air pumped at 400
148 mL min⁻¹ for continuous H₂O₂ production. The two electrodes of 3 cm² geometric area were
149 mounted as described earlier (Murillo-Sierra et al., 2018), with a separation of about 1 cm². In
150 photoassisted trials, a mirror was placed at the bottom of the tank reactor for a better photon
151 collection. An Agilent 6552A galvanostat, which continuously monitored the cell voltage, was
152 employed to ensure constant current density (j). Before the assays, 130 mL of a 0.050 M Na₂SO₄
153 solution was added to the cell and an electrolysis at $j = 100 \text{ mA cm}^{-2}$ was run for 180 min in order
154 to remove the surface impurities and activate the electrodes.

155 The AO-H₂O₂, homogeneous EF and EF-vermiculite trials were carried out in the dark. In
156 homogeneous EF, a concentration close to that of Fe²⁺ dissolved after 360 min of stirring of 1.0 g
157 L⁻¹ sodium vermiculite suspension in 0.050 M Na₂SO₄ at pH 3.0 and 25 °C was used. In PEF-
158 vermiculite, the solution was illuminated with a 6 W UVA lamp (Philips TL2001 fluorescent) that
159 provided 5.0 W m⁻² irradiance. The SPEF-vermiculite assays were made in clear and sunny days
160 of August, 2018 in Barcelona (Spain), with an average UV power of 36.2 W m⁻².

161 3.4. Analytical procedures

162 The solution pH was monitored with a Crison GLP 22 pH-meter. Fe²⁺ concentration in
163 solution was determined at $\lambda = 510$ nm via direct reaction with 1,10-phenanthroline. No other
164 metal ions (e.g., Mg²⁺, Al³⁺) present in the clay were analyzed because they are innocuous species
165 that do not yield any oxidizing species. In Fenton-based EAOPs, a drop of 1 M NaOH was added
166 to withdrawn samples to increase the pH and stop the degradation process. Then, they were filtered
167 with a 45- μ m PTFE filter from Whatman before analysis. The decolorization of the Ponceau SS
168 solution was followed from the absorbance decay at the maximum absorption wavelength ($\lambda_{\text{max}} =$
169 514 nm) using a Shimadzu1800 UV/Vis spectrophotometer. Samples were diluted (1:5) before
170 analysis. The percentage of color removal was calculated from Eq. (3):

$$171 \quad \% \text{ Color removal} = \frac{A_0 - A}{A_0} 100 \quad (3)$$

172 where A_0 and A denote the initial absorbance and that at electrolysis time t , respectively.

173 The mineralization of the diazo dye solutions was monitored from their TOC abatement with
174 a Shimadzu TOC-VCSN analyzer. An aliquot of 50 μ L was injected into the analyzer and the non-
175 purgeable organic content (NPOC) was measured with $\pm 1\%$ reproducibility.

176 The generated carboxylic acids were analyzed by ion-exclusion HPLC by injecting 10 μ L
177 aliquots into a Waters 600 liquid chromatograph, equipped with a Bio-Rad Aminex HPX 87H (300
178 mm \times 7.8 mm) column at 35 °C and a Waters 996 photodiode detector selected at $\lambda = 210$ nm.

179 Chromatograms were obtained by eluting 4 mM H₂SO₄ at 0.6 mL min⁻¹ and defined peaks were
180 displayed at retention times of 6.7, 7.7, 9.3, 9.6 and 15.2 min for oxalic, tartronic, oxamic, malic
181 and acetic acid, respectively.

182 All the assays were replicated and the average values are given. The figures contain the error
183 bars with a 95% confidence interval.

184 The morphology of the conditioned sodium vermiculite powder was studied by scanning
185 electron microscopy (SEM) using a JEOL JSM7100F microscope. Its chemical composition was
186 determined by energy dispersive X-ray spectroscopy (EDS) with an Oxford Instruments INCA
187 200 detector coupled to the microscope. The concentration of iron in solution was measured by
188 inductively coupled plasma-mass spectrometry (ICP-MS) using a Perkin Elmer Elan-6000
189 spectrometer. NH₄⁺ concentration was obtained from the standard phenate method. NO₂⁻ and NO₃⁻
190 concentrations were determined by ion chromatography, using the procedures reported earlier
191 (Coria et al., 2018; dos Santos et al., 2018a).

192 **3. Results and discussion**

193 *3.1. Analysis of the sodium vermiculite sample*

194 Fig. SM-1 gathers several SEM images, at different magnifications, of the modified sodium
195 vermiculite used as heterogeneous catalyst in this work. It was composed of particles of irregular
196 size, typically lower than 14 μm. However, they tended to agglomerate once suspended and stirred
197 to perform the electrolyses, ending in particles bigger than 45 μm. As mentioned in previous
198 section, microfiltration allowed their removal prior to all the analyses. EDS analysis in Fig. SM-2
199 reveals the presence of Si, Mg and Al as main components, along with a minor proportion of Fe,
200 K and Na, as expected from the origin of this natural mineral. From this analysis, the composition
201 of the sample, expressed in the form of oxides, was determined and the results obtained are
202 collected in Table SM-3. It is worth noting the high percentage in weight of Fe (as FeO) contained

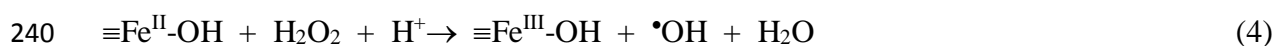
203 in the solid catalyst (8.68 wt.%), thus becoming a promising candidate for heterogeneous Fenton-
204 based EAOPs. The X-ray diffraction (XRD) pattern, Fourier transform infrared (FTIR) spectra, X-
205 ray fluorescence analysis, UV/Vis diffuse reflectance spectra between 200 and 600 nm, specific
206 area determined by the Brunauer–Emmett–Teller (BET) method and thermogravimetric analysis
207 of the catalyst have been reported in earlier work (Batista et al., 2019).

208 The stability of sodium vermiculite in aqueous medium was determined by suspending this
209 material at 1.0 g L⁻¹ in 0.050 M Na₂SO₄ solutions at pH 3.0, 7.0 and 10.0, and 25 °C. After 360
210 min of vigorous stirring, no significant pH change was observed. At pH 7.0 and 10.0, iron traces
211 (< 10⁻³ mM) were detected in the final solutions, whereas a very small iron content of 0.015 mM
212 was determined at pH 3.0. This resulted from the corrosion of the sodium vermiculite particles
213 upon chemical attack by H⁺ ions. The iron leaching was relatively low, which can be explained by
214 the fact that it is covalently bound to the mineral layers (Purceno et al., 2012). Note that the amount
215 of iron ions released to the bulk solution at pH 3.0 is much lower than 0.50 mM Fe²⁺ typically
216 added as catalyst in homogeneous Fenton-based EAOPs using an air-diffusion cathode (Brillas et
217 al., 2009; Sirés et al., 2014, dos Santos et al., 2018a). Therefore, a large catalytic activity of sodium
218 vermiculite in the heterogeneous EAOPs to be performed would point out to the prevailing role of
219 a heterogeneous degradation mechanism.

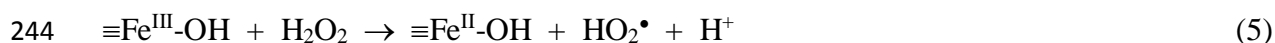
220 *3.2. Decolorization of Ponceau SS solutions by heterogeneous EAOPs*

221 A blank was first made with 130 mL of 0.150 mM Ponceau SS in 0.050 M Na₂SO₄ at pH 3.0
222 and 25 °C, in the presence of 1.0 g L⁻¹ sodium vermiculite. The suspension was vigorously stirred
223 in the dark for 360 min. As can be seen in Fig. 1a, only 0.61% of color was finally removed,
224 suggesting that the diazo dye adsorption onto the catalyst particles was irrelevant. Hence, the dye
225 degradation achieved in the electrochemical treatments shown in Fig. 1a is mainly caused by the
226 generated •OH. No significant pH changes were found during these trials.

227 In Fig. 1a, it is evident that AO-H₂O₂ with a BDD/air diffusion cell yielded the poorest
 228 decontamination among all electrochemical trials under study, achieving 74.3% of color removal
 229 after 360 min at $j = 33.3 \text{ mA cm}^{-2}$. This color disappearance resulted from the attack of BDD($\bullet\text{OH}$)
 230 formed from reaction (1) and, to a lesser extent, H₂O₂ produced at the cathode (Brillas and
 231 Martínez-Huitle, 2015). A comparative homogeneous EF process with 0.018 mM Fe²⁺, close to
 232 the concentration found after 360 min of suspension stirring without current supply, was also run.
 233 This process led to a slightly superior color removal as compared to AO-H₂O₂, attaining 80.0% of
 234 decolorization, which can be explained by the additional oxidation of the target molecule and its
 235 colored products by $\bullet\text{OH}$ originated from homogeneous Fenton's reaction (2). The color removal
 236 was much faster by EF-vermiculite process with 1.0 g L⁻¹ of heterogeneous catalyst, attaining
 237 92.4% decolorization. The enhanced color loss as compared to homogeneous EF suggests a larger
 238 oxidation promoted by $\bullet\text{OH}$ formed at the surface of the clay particles by the following
 239 heterogeneous Fenton's reaction (4) (Ganiyu et al., 2018):



241 where $\equiv\text{Fe}^{\text{II}}\text{-OH}$ and $\equiv\text{Fe}^{\text{III}}\text{-OH}$ denote the Fe(II) and Fe(III) species on the catalyst surface,
 242 respectively. The former can be regenerated from the heterogeneous Fenton-like reaction (5) by
 243 the excess of H₂O₂ produced, yielding the weaker oxidant hydroperoxyl radical (HO₂ \bullet):



245 By comparing the relative increase of decolorization percentage in homogeneous EF and EF-
 246 vermiculite (5.7% vs. 18.1% as compared to AO-H₂O₂), one can conclude that the contribution of
 247 $\bullet\text{OH}$ from Fenton-based routes to overall loss of color of the Ponceau SS solution in EF-vermiculite
 248 process could be divided into: homogeneous $\bullet\text{OH}$ (~ 32% of Fenton's contribution) and
 249 heterogeneous $\bullet\text{OH}$ (~ 68%). Fig. 1a also highlights that the decolorization was enhanced by PEF-
 250 vermiculite, being even faster in SPEF-vermiculite. These two processes allowed reaching total

251 color removal in 300-360 min. The superiority of photoassisted processes can be explained by the
252 additional production of $\bullet\text{OH}$ from the photolysis of the hydrolyzed homogeneous Fe(III) and
253 heterogeneous $\equiv\text{Fe}^{\text{III}}\text{-OH}$ species, highly photoactive at pH 3.0 (Brillas et al., 2009; Sirés et al.,
254 2014; dos Santos et al., 2018a). SPEF-vermiculite yielded the best results due to the greater
255 irradiance from sunlight, which enhanced all the photolytic reactions.

256 The absorbance decays determined for the above experiments agreed with a pseudo-first-order
257 kinetics, as presented in Fig. 1b. Good linear fittings can be observed in all cases, corresponding
258 the slope to the apparent rate constant for decolorization (k_{dec}). Table 1 summarizes the k_{dec} -values
259 obtained, which always show excellent R -squared values (≥ 0.989). As expected, the k_{dec} -value
260 increased with the oxidation ability of the EAOP, from $3.52 \times 10^{-3} \text{ min}^{-1}$ for the weak AO- H_2O_2 to
261 $1.40 \times 10^{-2} \text{ min}^{-1}$ for the powerful SPEF-vermiculite at $j = 33.3 \text{ mA cm}^{-2}$. This simple kinetics
262 suggests the production of a small and constant quantity of homogeneous and/or heterogeneous
263 $\bullet\text{OH}$ in each treatment.

264 3.3. Mineralization of Ponceau SS solutions by heterogeneous EAOPs

265 Fig. 2a depicts the TOC abatement with electrolysis time for the assays discussed in Fig. 1a.
266 A larger mineralization was achieved in good agreement with the sequence observed for the
267 decolorization profile in each EAOP: AO- $\text{H}_2\text{O}_2 <$ homogeneous EF $<$ EF-vermiculite $<$ PEF-
268 vermiculite $<$ SPEF-vermiculite. Table 1 lists the corresponding TOC abatement achieved after
269 360 min of electrolysis, which progressively rose from 40.2% in AO- H_2O_2 to 84.1% in SPEF-
270 vermiculite. The lower extent of mineralization as compared to decolorization can be accounted
271 for by a slower attack of BDD($\bullet\text{OH}$) and/or homogeneous and heterogeneous $\bullet\text{OH}$ formed via
272 Fenton-based reactions onto degradation products. These compounds were more largely
273 mineralized by the homogeneous $\bullet\text{OH}$ formed from Fenton's reaction (2) in homogeneous EF, as
274 compared to AO- H_2O_2 that only counted on the action of BDD($\bullet\text{OH}$). The greater TOC removal

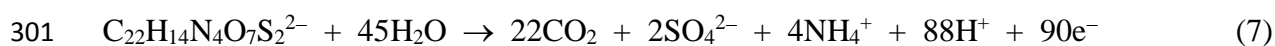
275 attained in EF-vermiculite corroborates the large oxidation ability of heterogeneous $\bullet\text{OH}$ produced
 276 from heterogeneous Fenton's reaction (4). When compared to AO- H_2O_2 , the final TOC decay at
 277 360 min was upgraded by 8% in homogeneous EF and 17% in EF-vermiculite. Therefore, within
 278 the Fenton-based mineralization routes occurring in the latter process, a slightly greater
 279 contribution ($\sim 53\%$) corresponded to heterogeneous EF. The partial TOC removals inform about
 280 the generation of products that are very refractory to either BDD($\bullet\text{OH}$) or $\bullet\text{OH}$. The enhancement
 281 found in the photoassisted methods (PEF-vermiculite and SPEF-vermiculite) can then be related
 282 not only to the production of larger amounts of $\bullet\text{OH}$ from the photolysis of homogeneous and
 283 heterogeneous Fe(III) species, but also to the fast photodecomposition of refractory intermediates.
 284 The latter reactions involve, for example, the photolysis of Fe(III) complexes formed with the final
 285 short-chain carboxylic acids (Sirés et al., 2014), as discussed below. The greater UV irradiance
 286 from sunlight as compared to the UVA lamp justifies that the maximum mineralization was
 287 attained by SPEF-vermiculite process.

288 It is well known that the $-\text{SO}_3^-$ groups of azo dyes are completely released as SO_4^{2-} ion during
 289 their mineralization process (Brillas and Martinez-Huitle, 2015). On the other hand, the analysis
 290 of nitrogenated ions in the 0.150 mM Ponceau SS solution after 360 min of electrolysis by PEF-
 291 vermiculite at pH 3.0 and $j = 33.3 \text{ mA cm}^{-2}$ revealed an accumulation of 0.258 mM of NH_4^+ ion
 292 (43.0% of 0.60 mM of initial N), without formation of NO_2^- and NO_3^- ions. From this finding, the
 293 percentage of mineralization current efficiency (MCE) in each treatment at a given current I (in
 294 A) was estimated from Eq. (6) (dos Santos et al., 2018a):

$$295 \text{MCE} = \frac{n F V \Delta\text{TOC}}{4.32 \times 10^7 m I t} 100 \quad (6)$$

296 where V is the solution volume (in L) and ΔTOC is the destroyed solution TOC (in mg L^{-1}) at
 297 time t (in h). The constant parameters in Eq. (6) were: 4.32×10^7 as a unit homogenization factor
 298 ($= 3600 \text{ s h}^{-1} \times 12000 \text{ mg C mol}^{-1}$) and the number of carbon atoms of the diazo dye, $m = 22$. The

299 number of consumed electrons was $n = 90$, considering the total mineralization of the soluble
300 dianionic form of Ponceau SS to CO_2 and SO_4^{2-} and NH_4^+ ions, according to reaction (7):



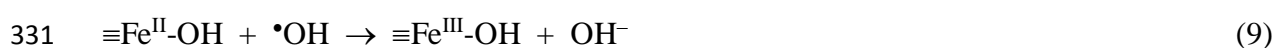
302 Eq. (6) reveals that a greater MCE value can be attained as ΔTOC becomes higher when the
303 same I is applied, which is feasible as the EAOP presents a greater oxidation ability. This trend
304 can be observed in Fig. 2b, which shows the MCE values obtained for the experiments of Fig. 2a,
305 as well as in the last column of Table 1 that collects such data at 360 min of each treatment. Fig.
306 2b shows steady MCE values after 120-180 min in AO- H_2O_2 , homogeneous EF and EF-
307 vermiculite, suggesting a constant mineralization rate of products formed. In contrast, the MCE
308 value decayed drastically in PEF-vermiculite (from 14.7% to 6.1%), and more dramatically in the
309 potent SPEF-vermiculite (from 23.7% to 6.7%). This can be attributed to the progressive
310 generation of more recalcitrant products that are hardly destroyed by hydroxyl radicals and UVA
311 light or sunlight.

312 *3.4. Effect of experimental variables on the photoelectro-Fenton-vermiculite process*

313 The effect of the main experimental variables, namely catalyst content, current density and
314 diazo dye concentration, on the performance of the heterogeneous Fenton-based EAOPs in 0.050
315 M Na_2SO_4 at pH 3.0 using a BDD/air diffusion cell was assessed for the PEF-vermiculite process.
316 Similar conclusions are expected for EF-vermiculite and SPEF-vermiculite since they generated
317 the same kind of oxidizing species.

318 The effect of sodium vermiculite concentration, from 0.25 to 2.0 g L^{-1} , on color disappearance
319 for the treatment of 130 mL of 0.150 mM diazo dye at $j = 33.3 \text{ mA cm}^{-2}$ is shown in Fig. 3a. After
320 360 min of electrolysis, the percentage of color removal grew gradually from 92.3% at 0.25 g L^{-1}
321 to total decolorization at 1.0 g L^{-1} , whereas at greater content like 2.0 g L^{-1} it dropped down to
322 97.2%. The same trend can be observed for the corresponding k_{dec} -values given in Table 1, with a

323 maximal of $1.23 \times 10^{-2} \text{ min}^{-1}$ at 1.0 g L^{-1} sodium vermiculite. The faster removal upon initial
324 increase of sodium vermiculite content can be ascribed to the promotion of the homogeneous and
325 heterogeneous Fenton's reactions because of the larger amounts of dissolved Fe^{2+} and immobilized
326 $\equiv\text{Fe}^{\text{II}}\text{-OH}$. The subsequent decrease in percentage of color removal at 2.0 g L^{-1} sodium vermiculite
327 can be explained by the partial destruction of homogeneous and heterogeneous $\bullet\text{OH}$ upon
328 occurrence of parasitic homogeneous reaction (8) and heterogeneous reaction (9) (Sirés et al.,
329 2014).



332 The same tendency can be observed in Fig. 3b for the TOC decay during the same assays. The
333 highest mineralization rate was reached again at 1.0 g L^{-1} sodium vermiculite, with a TOC
334 reduction of 76.9% (see Table 1). This was consistent with the corresponding MCE values (see
335 Fig. 3c and Table 1), which became maximal for that experiment. Note that, up to 0.50 g L^{-1} , Fig.
336 3c shows a practically steady profile of MCE curves, whereas it decayed largely over time at
337 greater sodium vermiculite contents. This latter behavior suggests the production of larger amounts
338 of homogeneous and heterogeneous $\bullet\text{OH}$, favoring the initial degradation of the most oxidizable
339 products followed by the accumulation of more persistent pollutants, eventually causing a drastic
340 MCE drop as shown in Fig. 3c. A sodium vermiculite concentration of 1.0 g L^{-1} was then selected
341 to carry out the subsequent experiments.

342 The current density determines the production of oxidizing agents in the PEF-vermiculite
343 process. An increase in j is expected to accelerate the electrode reactions, thus generating more
344 BDD($\bullet\text{OH}$) as well as H_2O_2 that, in turn, may produce larger amounts of homogeneous and
345 heterogeneous $\bullet\text{OH}$ from Fenton-based reactions (Panizza and Cerisola, 2009; Sirés et al., 2014;
346 Ganiyu et al., 2018). This behavior can be confirmed in Fig. 4a for the color removal during the

347 treatment of 0.150 mM Ponceau SS at 16.6-66.6 mA cm⁻². Only 88.6% of color disappeared at the
348 end of the trial at $j = 16.6$ mA cm⁻², whereas total decolorization was reached after 360 min at $j =$
349 33.3 mA cm⁻² and after 300 min at $j = 66.6$ mA cm⁻². These trends can also be seen in Table 1
350 from the gradual rise of the k_{dec} -value obtained in these assays, attaining a maximal of 1.74×10^{-2}
351 min⁻¹ at $j = 66.6$ mA cm⁻². Similarly, Fig. 4b highlights a higher TOC abatement at greater j ,
352 growing the mineralization degree from 48.7% to 84.5% when j was risen from 16.6 to 66.6 mA
353 cm⁻². This confirms that the enhancement in \bullet OH production was beneficial to oxidize the organics.
354 In contrast, the profiles of Fig. 4c show an opposite trend for MCE, which gradually dropped as j
355 was increased (see also its value at 360 min in Table 1). This is a typical finding in homogeneous
356 EAOPs and it is also verified here for heterogeneous EAOPs. It is due to the relative loss of
357 oxidants available to react with organics, owing to the concomitant acceleration of their parasitic
358 reactions. Among them, the most usual include the oxidation of BDD(\bullet OH) to O₂ and the reaction
359 of \bullet OH with H₂O₂ giving rise to the weaker oxidant HO₂ \bullet (Brillas et al., 2009; Panizza and
360 Cerisola, 2009). Low j values are then preferred to develop a more efficient treatment, although at
361 the expense of a slower TOC abatement.

362 The influence of the diazo dye concentration on the performance of the PEF-vermiculite
363 treatment was studied between 0.075 and 2.25 mM Ponceau SS at $j = 33.3$ mA cm⁻². As can be
364 seen in Fig. 5a, greater decolorization rate was obtained at lower diazo dye content, attaining total
365 color loss after 300 min for the most diluted solution, but only 80.8% removal at 360 min for the
366 most concentrated. The k_{dec} -value in the former assay was 4.7-fold higher than in the latter one,
367 whose content was 3 times greater (see Table 1). This can be related to the formation of analogous
368 amounts of oxidizing agents at all dye concentrations, being easier to destroy a lower number of
369 organic molecules. Nevertheless, the much superior k_{dec} -value determined at 0.075 mM as
370 compared to 2.25 mM suggests that the heterogeneous degradation occurred in concomitance with
371 a slight diazo dye adsorption (see Fig. 1a), with saturation of the active centers (\equiv Fe^{II}-OH and

372 $\equiv\text{Fe}^{\text{III}}\text{-OH}$) of the catalyst particles. This facilitated the removal of low Ponceau SS concentrations,
373 favoring the destruction at the catalyst surface. The same behavior can be observed in Fig. 5b for
374 the corresponding TOC removal, which reached an almost total mineralization of 94.4% at 0.075
375 mM, whereas only 41.3% was attained at 2.25 mM (see Table 1). However, the MCE profiles
376 depicted in Fig. 5c show an anomalous tendency, with maximum values at 0.150 mM Ponceau SS
377 and similar efficiencies at 0.075 and 0.225 mM. In homogeneous EAOPs, a gradual rise of MCE
378 as the target molecule content is increased is typically found, due to the deceleration of parasitic
379 reactions that consume hydroxyl radicals, which allows their faster attack onto the organics
380 (Oturán and Aaron, 2014; Sirés et al., 2014). The fact that similar MCE values were obtained at
381 the lowest and highest dye concentrations could be explained by the adsorption of organic
382 molecules on the particles surface, as pointed out above, favoring the destruction of the smaller
383 concentrations. It can then be considered that concentrations higher than 0.150 mM Ponceau SS
384 are excessive for the selected catalyst content in PEF-vermiculite treatment.

385 The reproducibility was tested by reusing a given sample of sodium vermiculite catalyst at a
386 concentration of 1 g L^{-1} (collected by filtration) to consecutively degrade 130 mL of 0.150 mM
387 Ponceau SS solutions with 0.050 M Na_2SO_4 at pH 3.0 and 25 °C by PEF-vermiculite at 33.3 mA
388 cm^{-2} for 360 min. The percentage of TOC removal achieved at the end of the 5th cycle was 74.7%,
389 only 2.9% lower than 76.9% TOC decay obtained in the 1st cycle (see Table 1). This means that
390 sodium vermiculite was quite stable, being successfully reused for consecutive heterogeneous
391 treatments of the dye solution.

392 *3.5. Time course of final short-chain linear carboxylic acids*

393 The mineralization of azo dyes usually leads to the generation of short-chain linear carboxylic
394 acids as final products (Brillas and Martínez-Huitle, 2015; dos Santos et al., 2018a). This was
395 corroborated from ion-exclusion HPLC analysis of the 0.150 mM Ponceau SS solution treated by
396 PEF-vermiculite with 1.0 g L^{-1} catalyst at $j = 33.3 \text{ mA cm}^{-2}$. Fig. 6 presents the evolution of oxalic,

397 oxamic, malic, tartronic and acetic acids detected. The three latter acids were formed from the
398 cleavage of aromatic products and degradation of longer carboxylic acids, further being oxidized
399 to oxalic acid. The destruction of N-products led to the formation of oxamic acid. This acid and
400 oxalic acid are final products since they are directly converted into CO₂. All these carboxylic acids
401 form Fe(III) complexes that are easily photolyzed under UVA light irradiation (Sirés et al., 2014),
402 thereby enhancing the mineralization process. Fig. 6 highlights that oxalic acid was the most
403 abundant acid, being accumulated up to 21.2 mg L⁻¹ at 180 min and rapidly decaying down to 3.9
404 mg L⁻¹ at 360 min because of the fast decomposition of Fe(III)-oxalate complexes. At the end of
405 the process, 1.9, 0.5 and 6.5 mg L⁻¹ of oxamic, malic and tartronic acids were found, whereas
406 acetic acid disappeared completely. All these acids accounted for 3.8 mg L⁻¹ TOC, only
407 representing a 17.4% of the 23.1 mg L⁻¹ TOC contained in the final solution (see Fig. 2a). This
408 means that more persistent products were largely accumulated at the end of the PEF-vermiculite
409 process, being very slowly destroyed by hydroxyl radicals and/or UV radiation.

410 **4. Conclusions**

411 Microparticles of a modified clay mineral like sodium vermiculite can be effectively employed
412 as catalyst in heterogeneous Fenton-based water treatments such as EF-vermiculite, PEF-
413 vermiculite and SPEF-vermiculite. A galvanostatic study was carried out using 0.150 mM Ponceau
414 SS solutions at pH 3.0 in a BDD/air diffusion cell to assess the performance of these novel
415 methods. The decolorization and mineralization processes involved the attack of BDD([•]OH), as
416 well as [•]OH formed from homogeneous and heterogeneous Fenton's reactions. The homogeneous
417 Fenton process occurred upon leaching of small amounts of iron ions, but its role was much less
418 relevant than heterogeneous process favored by Fe^{II}-OH species bound to the clay mineral layers.
419 The photoassisted treatments had higher oxidation power than EF-vermiculite because of the very
420 positive action of UV photons on degradation products. The most powerful process was SPEF-

421 vermiculite, yielding total color removal and 84.1% mineralization at $j = 33.3 \text{ mA cm}^{-2}$. Oxalic,
422 oxamic, malic, tartronic and acetic acids were detected as final short-linear carboxylic acids during
423 the PEF-vermiculite treatments.

424 Based on the promising results found in the present work, the heterogeneous Fenton-based
425 treatments with sodium vermiculite as catalyst are currently in progress, testing their performance
426 for other dyes at neutral pH aiming to expand the applicability to a wider pH range. That study
427 includes the characterization of the clay mineral, before and after use, by conventional
428 physicochemical techniques that are expected to shed light on the catalyst stability.

429 **Acknowledgements**

430 Financial support from project CTQ2016-78616-R (AEI/FEDER, EU) and projects CNPq –
431 465571/2014-0, CNPq - 446846/2014-7 and CNPq - 401519/2014-7T (National Council for
432 Scientific and Technological Development, Brazil) is acknowledged A.J. dos Santos
433 acknowledges funding from CAPES (Brazil) through program “Pesquisa Pós-doutoral no
434 Exterior” number 88881.172332/2018-01.

435 **References**

- 436 Batista, L.M.B., Bezerra, F.A., Oliveira, J.L.F., Araújo. A.M.M., Fernandes Jr., V.J., Araujo, A.S..
437 Gondim, A.D., Alves, A.P.M., 2019. Pyrolysis of glycerol with modified vermiculite catalysts.
438 Kinetic and PY-GC/MS. *J. Therm. Anal. Calorim.* DOI: [https://doi.org/10.1007/s10973-019-](https://doi.org/10.1007/s10973-019-08083-1)
439 08083-1.
- 440 Bezerra Rocha, J.H., Sales Solano, A.M., Fernandes, N.S., Ribeiro da Silva, D., Peralta-
441 Hernández, J.M., Martínez-Huitle, C.A., 2012. Electrochemical degradation of Remazol Red
442 BR and Novacron Blue C-D dyes using diamond electrode. *Electrocatalysis* 3, 1–12.

443 Bhattacharya, B., Sanghi, R., 2003. Adsorption-coagulation for the decolorisation of textile dye
444 solutions. *Water Qual. Res. J. Can.* 38, 553–562.

445 Boye, B., Michaud, P.A., Marselli, B., Dieng, M.M., Brillas, E., Comninellis, C., 2002. Anodic
446 oxidation of 4-chlorophenoxyacetic acid on synthetic boron-doped diamond electrodes, *New*
447 *Diamond Frontier Carbon Technol.* 12, 63-72.

448 Brillas, E., 2014. A review on the degradation of organic pollutants in waters by UV photoelectro-
449 Fenton and solar photoelectro-Fenton. *J. Braz. Chem. Soc.* 25, 393–417.

450 Brillas, E., Martínez-Huitle, C.A., 2015. Decontamination of wastewaters containing synthetic
451 organic dyes by electrochemical methods. An updated review. *Appl. Catal. B: Environ.* 166-
452 167, 603–643.

453 Brillas, E., Sirés, I., Oturan, M.A., 2009. Electro-Fenton and related electrochemical technologies
454 based on Fenton’s reaction chemistry. *Chem. Rev.* 109, 6570–6631.

455 Chen, Q., Wu, P., Dang, Z., Zhu, N., Li, P., Wu, J., Wang, X., 2010. Iron pillared vermiculite as a
456 heterogeneous photo-Fenton catalyst for photocatalytic degradation of azo dye reactive
457 brilliant orange X-GN. *Sep. Purif. Technol.* 71, 315–323.

458 Coria, G., Pérez, T., Sirés, I., Brillas, E., Nava, J.L., 2018. Abatement of the antibiotic levofloxacin
459 in a solar photoelectro-Fenton flow plant: modeling the dissolved organic carbon
460 concentration-time relationship. *Chemosphere* 198, 174–181.

461 Coria, G., Pérez, T., Sirés, I., Nava, J.L., 2015. Mass transport studies during dissolved oxygen
462 reduction to hydrogen peroxide in a filter-press electrolyzer using graphite felt, reticulated
463 vitreous carbon and boron-doped diamond as cathodes. *J. Electroanal. Chem.* 757, 225–229.

464 Coria, G., Sirés, I., Brillas, E., Nava, J.L., 2016. Influence of the anode material on the degradation
465 of naproxen by Fenton-based electrochemical processes. *Chem. Eng. J.* 304, 817–825.

466 dos Santos, A.B., Cervantes, F.J., van Lier, J.B., 2007. Review paper on current technologies for
467 decolourisation of textile wastewaters: perspectives for anaerobic biotechnology. *Bioresour.*
468 *Technol.* 98, 2369–2385.

469 dos Santos, A.J., Martínez-Huitle, C.A., Sirés, I., Brillas, E., 2018a. Use of Pt and BDD anodes in
470 the electrochemical advanced oxidation of Ponceau SS diazo dye in acidic sulfate medium.
471 *ChemElectroChem* 5, 685–693.

472 dos Santos, A.J., Sirés, I., Martínez-Huitle, C.A., Brillas, E., 2018b. Total mineralization of
473 mixtures of Tartrazine, Ponceau SS and Direct Blue 71 azo dyes by solar photoelectro-
474 Fenton in pre-pilot plant. *Chemosphere* 210, 1137–1144.

475 Dominguez, C.M., Oturan, N., Romero, A., Santos, A., Oturan, M.A., 2018. Removal of lindane
476 wastes by advanced electrochemical oxidation. *Chemosphere* 202, 400–409.

477 Ellouze, S., Kessemtni, S., Clematis, D., Cerisola, G., Panizza, M., Chaâbane Elaoud, S., 2017.
478 Application of Doehlert design to the electro-Fenton treatment of Bismarck Brown Y. J.
479 *Electroanal. Chem.* 799, 34–39.

480 Fajardo, A.S., dos Santos, A.J., de Araújo Costa, E.C.T., da Silva, D.R., Martínez-Huitle, C.A.,
481 2019. Effect of anodic materials on solar photoelectro-Fenton process using a diazo dye as
482 a model contaminant. *Chemosphere* 225, 880–889.

483 Ferma Group, 2019. <http://www.ferbagroup.com/vermiculite/> (accessed in 2019).

484 Flores, N., Brillas, E., Centellas, F., Rodríguez, R.M., Cabot, P.L., Garrido, J.A., Sirés, I., 2018.
485 Treatment of olive oil mill wastewater by single electrocoagulation with different electrodes
486 and sequential electrocoagulation/electrochemical Fenton-based processes. *J. Hazard.*
487 *Mater.* 347, 58–66.

488 Galia, A., Lanzalaco, S., Sabatino, M.A., Dispenza, C., Scialdone, O., Sirés, I., 2016. Crosslinking
489 of poly(vinylpyrrolidone) activated by electrogenerated hydroxyl radicals: A first step

490 towards a simple and cheap synthetic route of nanogel vectors. *Electrochem. Commun.* 62,
491 64–68.

492 Ganiyu, S.O., Zhou, M., Martínez-Huitile, C.A., 2018. Heterogeneous electro-Fenton and
493 photoelectro-Fenton processes: a critical review of fundamental principles and application
494 for water/wastewater treatment. *Appl. Catal. B: Environ.* 235, 103–129.

495 Ganzenko, O., Oturan, N., Sirés, I., Huguenot, D., van Hullebusch, E.D., Esposito, G., Oturan,
496 M.A., 2018. Fast and complete removal of the 5-fluorouracil drug from water by electro-
497 Fenton oxidation. *Environ. Chem. Lett.* 16, 281–286.

498 Hafaiedh, N.B., Fourcade, F., Bellakhal, N., Amrane, A., 2018. Iron oxide nanoparticles as
499 heterogeneous electro-Fenton catalysts for the removal of AR18 azo dye. *Environ. Technol.*
500 DOI: 10.1080/09593330.2018.1557258.

501 Lanzalaco, S., Sirés, I., Galia, A., Sabatino, M.A., Dispenza, C., Scialdone, O., 2018. Facile
502 crosslinking of poly(vinylpyrrolidone) by electro-oxidation with IrO₂-based anode under
503 potentiostatic conditions. *J. Appl. Electrochem.* 48, 1343–1352.

504 Lanzalaco, S., Sirés, I., Sabatino, M.A., Dispenza, C., Scialdone, O., Galia, A., 2017. Synthesis of
505 polymer nanogels by electro-Fenton process: investigation of the effect of main operation
506 parameters. *Electrochim. Acta* 246, 812–822.

507 Lee, W.J., Batchelor, B., 2004. Abiotic reductive dechlorination of chlorinated ethylenes by iron-
508 bearing phyllosilicates. *Chemosphere* 56, 999–1009.

509 Liu, Y., Li, H., Tan, G.Q., Zhu, X.H., 2011. Fe²⁺-modified vermiculite for the removal of
510 chromium (VI) from aqueous solution. *Sep. Sci. Technol.* 46, 290–299.

511 Martínez-Costa, J.I., Rivera-Utrilla, J., Leyva-Ramos, R., Sánchez-Polo, M., Velo-Gala, I., 2018.
512 Individual and simultaneous degradation of antibiotics sulfamethoxazole and trimethoprim
513 by UV and solar radiation in aqueous solution using bentonite and vermiculite as
514 photocatalysts. *Appl. Clay Sci.* 160, 217–225.

515 Martínez-Costa, J.I., Rubio, M.I.M., Leyva-Ramos, R., 2019. Degradation of emerging
516 contaminants diclofenac, sulfamethoxazole, trimethoprim and carbamazepine by bentonite
517 and vermiculite at a pilot solar compound parabolic collector. *Catal. Today* (2019) DOI:
518 <https://doi.org/10.1016/j.cattod.2018.07.021>.

519 Martínez-Huitle, C.A., Rodrigo, M.A., Sirés, I., Scialdone, O., 2015. Single and coupled
520 electrochemical processes and reactors for the abatement of organic water pollutants: a
521 critical review. *Chem. Rev.* 115, 13362–13407.

522 Mascia, M., Vacca, A., Polcaro, S.M., Palmas, S., da Pozzo, A., 2011. Electrochemical treatment
523 of simulated ground water containing MTBE and BTEX with BDD anodes. *J. Chem.*
524 *Technol. Biotechnol.* 86, 128-137.

525 Murillo-Sierra, J.C., Sirés, I., Brillas, E., Ruiz-Ruiz, E.J., Hernández-Ramírez, A., 2018. Advanced
526 oxidation of real sulfamethoxazole + trimethoprim formulations using different anodes and
527 electrolytes. *Chemosphere* 192, 225–233.

528 Olvera-Vargas, H., Oturan, N., Oturan, M.A., Brillas, E., 2015. Electro-Fenton and solar
529 photoelectro-Fenton treatments of the pharmaceutical ranitidine in pre-pilot flow plant scale.
530 *Sep. Purif. Technol.* 146, 127–135.

531 Oturan, M.A., Aaron, J.J., 2014. Advanced oxidation processes in water/wastewater treatment:
532 principles and applications. A review. *Crit. Rev. Environ. Sci. Technol.* 44, 2577–2641.

533 Panizza, M., Cerisola, G., 2009. Direct and mediated anodic oxidation of organic pollutants. *Chem.*
534 *Rev.* 109, 6541–6569.

535 Panizza, M., Dirany, A., Sirés, I., Haidar, M., Oturan, N., Oturan, M.A., 2014. Complete
536 mineralization of the antibiotic amoxicillin by electro-Fenton with a BDD anode. *J. Appl.*
537 *Electrochem.* 44, 1327–1335.

538 Pérez, T., Sirés, I., Brillas, E., Nava, J.L., 2017. Solar photoelectro-Fenton flow plant modeling
539 for the degradation of the antibiotic erythromycin in sulfate medium. *Electrochim. Acta* 228,
540 45–56.

541 Polcaro, A.M., Mascia, M., Palmas, S., Vacca, A., 2003. Electrochemical oxidation of phenolic
542 and other organic compounds at boron doped diamond electrodes for wastewater treatment:
543 effect of mass transfer. *Ann. Chim.* 93, 987-976.

544 Polcaro, A.M., Vacca, A., Mascia, M., Palmas, S., 2007. Electrokinetic removal of 2,6-
545 dichlorophenol and diuron from kaolinite and humic acid-clay system. *J. Hazard. Mater.*
546 148, 505-512.

547 Poza-Nogueiras, V., Rosales, E., Pazos, M., Sanromán, M.A., 2018. Current advances and trends
548 in electro-Fenton process using heterogeneous catalysts – A review. *Chemosphere* 201, 399–
549 416.

550 Purceno, A.D., Teixeira, A.N.C., Souza, A.B., Ardisson, J.D., Mesquita, J.P., Lago, R.M., 2012.
551 Ground vermiculite as catalyst for the Fenton reaction. *Appl. Clay Sci.* 69, 87–92.

552 Rajkumar, D., Kim, J.G., 2006. Oxidation of various reactive dyes with in situ electrogenerated
553 active chlorine for textile dyeing industry wastewater treatment. *J. Hazard. Mater.* B136,
554 203–212.

555 Salazar, R., Brillas, E., Sirés, I., 2012. Finding the best Fe²⁺/Cu²⁺ combination for the solar
556 photoelectro-Fenton treatment of simulated wastewater containing the industrial textile dye
557 Disperse Blue 3. *Appl. Catal. B: Environ.* 115-116, 107–116.

558 Salazar, R., Garcia-Segura, S., Ureta-Zañartu, M.S., Brillas, E., 2011. Degradation of disperse azo
559 dyes from waters by solar photoelectro-Fenton. *Electrochim. Acta* 56, 6371-6379.

560 Santos, V., Morão, A., Pacheco, M.J., Ciríaco, L., Lopes, A., 2008. Electrochemical degradation
561 of azo dyes on BDD: effect of chemical structure and operating conditions on the combustion
562 efficiency. *J. Environ. Eng. Manage.* 18, 193–204.

563 Sharma, K.P., Sharma, S., Sharma, S.P., Singh, K., Kumar, S., Grover, R., Sharma, P.K., 2007. A
564 comparative study on characterization of textile wastewaters (untreated and treated) toxicity
565 by chemical and biological tests. *Chemosphere* 69, 48–54.

566 Sirés, I., Brillas, E., Oturan, M.A., Rodrigo, M.A., Panizza, M., 2014. Electrochemical advanced
567 oxidation processes: today and tomorrow. A review. *Environ. Sci. Pollut. Res.* 21, 8336–
568 8367.

569 Solís, M., Solís, A., Pérez, H.I., Manjarrez, N., Flores, M., 2012. Microbial decolouration of azo
570 dyes: a review. *Process Biochem.* 47, 1723–1748.

571 Steter, J.R., Brillas, E., Sirés, I., 2016. On the selection of the anode material for the
572 electrochemical removal of methylparaben from different aqueous media. *Electrochim. Acta*
573 222, 1464–1474.

574 Steter, J.R., Brillas, E., Sirés, I., 2018. Solar photoelectro-Fenton treatment of a mixture of
575 parabens spiked into secondary treated wastewater effluent at low input current. *Appl. Catal.*
576 B: *Environ.* 224, 410–418.

577 Thiam, A., Sirés, I., Brillas, E., 2015. Treatment of a mixture of food color additives (E122, E124
578 and E129) in different water matrices by UVA and solar photoelectro-Fenton. *Water Res.*
579 81, 178–187.

580 Ulson de Souza, S.M.A.G., Forgiarini, E., Ulson de Souza, A.A., 2007. Toxicity of textile dyes
581 and their degradation by the enzyme horseradish peroxidase (HRP). *J. Hazard. Mater.* 147,
582 1073–1078.

583 UNESCO, 2012. The United Nations World Water Development Report 4, Volume 1: Managing
584 Water Report under Uncertainty and Risk.

585 Verma, A.K., Dash, R.R., Bhunia, P., 2012. A review on chemical coagulation/flocculation
586 technologies for removal of colour from textile wastewaters. *J. Environ. Manage.* 93, 154–
587 168.

- 588 Ye, Z., Steter, J.R., Centellas, F., Cabot, P.L., Brillas, E., Sirés, I., 2019. Photoelectro-Fenton as
589 post-treatment for electrocoagulated benzophenone-3-loaded synthetic and urban
590 wastewater. *J. Clean. Prod.* 208, 1393–1402.
- 591 Yang, S., Wu, P., Ye, Q., Li, W., Chen, M., Zhu, N., 2018. Efficient catalytic degradation of
592 bisphenol A by novel Fe⁰-vermiculite composite in photo-Fenton system: mechanism and
593 effect of iron oxide shell. *Chemosphere* 208, 335–342.
- 594 Zollinger, H., 2003. *Color Chemistry: Synthesis, Properties, and Applications of Organic Dyes*
595 *and Pigments*, VHCA and Wiley-VCH, Switzerland.

596 **Figure captions**

597 **Fig. 1.** (a) Percentage of color removal vs. electrolysis time and (b) pseudo-first-order kinetic
598 analysis of absorbance decays for the treatment of 130 mL of 0.150 mM Ponceau SS solutions in
599 0.050 M Na₂SO₄ at pH 3.0 and 25 °C in a stirred cell with a 3 cm² boron-doped diamond (BDD)
600 anode and a 3 cm² air-diffusion cathode at current density (*j*) of 33.3 mA cm⁻². (●) Anodic
601 oxidation with electrogenerated H₂O₂ (AO-H₂O₂), (△) homogeneous electro-Fenton (EF) with
602 0.018 mM Fe²⁺, (■) EF-vermiculite, (▲) PEF-vermiculite and (▼) SPEF-vermiculite. In the three
603 latter methods, sodium vermiculite was suspended at 1.0 g L⁻¹ as catalyst. (◆) Loss of color with
604 the same sodium vermiculite concentration without current supply.

605 **Fig. 2.** Variation of (a) normalized TOC and (b) mineralization current efficiency with electrolysis
606 time for the assays of Fig. 1.

607 **Fig. 3.** Effect of the initial sodium vermiculite concentration on the change of (a) percentage of
608 color removal, (b) normalized TOC and (c) mineralization current efficiency with electrolysis time
609 for the PEF-vermiculite treatment of 130 mL of 0.150 mM Ponceau SS solutions in 0.050 M
610 Na₂SO₄ at pH 3.0 and 25 °C using a BDD/air-diffusion electrode cell at *j* = 33.3 mA cm⁻². [Sodium
611 vermiculite]: (●) 0.25 g L⁻¹, (■) 0.50 g L⁻¹, (▲) 1.0 g L⁻¹ and (◆) 2.0 g L⁻¹.

612 **Fig. 4.** Influence of current density on the variation of (a) percentage of color removal, (b)
613 normalized TOC and (c) mineralization current efficiency with electrolysis time for the PEF-
614 vermiculite treatment of 130 mL of a 0.150 mM Ponceau SS solution in 0.050 M Na₂SO₄ with 1.0
615 g L⁻¹ sodium vermiculite at pH 3.0 and 25 °C using a BDD/air-diffusion electrode cell. Current
616 density: (●) 16.6 mA cm⁻², (▲) 33.3 mA cm⁻² and (■) 66.6 mA cm⁻².

617 **Fig. 5.** Effect of Ponceau SS content on (a) percentage of color removal, (b) normalized TOC and
618 (c) mineralization current efficiency vs. electrolysis time for the PEF-vermiculite treatment of 130
619 mL of diazo dye solutions with 0.050 M Na₂SO₄ and 1.0 g L⁻¹ sodium vermiculite at pH 3.0 and

620 25 °C using a BDD/air-diffusion electrode cell at $j = 33.3 \text{ mA cm}^{-2}$. [Ponceau SS]₀: (◆) 0.075 mM,
621 (▲) 0.150 mM and (▼) and 0.225 mM.

622 **Fig. 6.** Time course of the concentration of (●) oxalic, (■) oxamic, (▼) malic, (◆) tartronic and
623 (▲) acetic acids detected during the PEF-vermiculite treatment of 130 mL of a 0.150 mM Ponceau
624 SS solution in 0.050 M Na₂SO₄ with 1.0 g L⁻¹ sodium vermiculite at pH 3.0 and 25 °C using a
625 BDD/air-diffusion electrode cell at $j = 33.3 \text{ mA cm}^{-2}$.

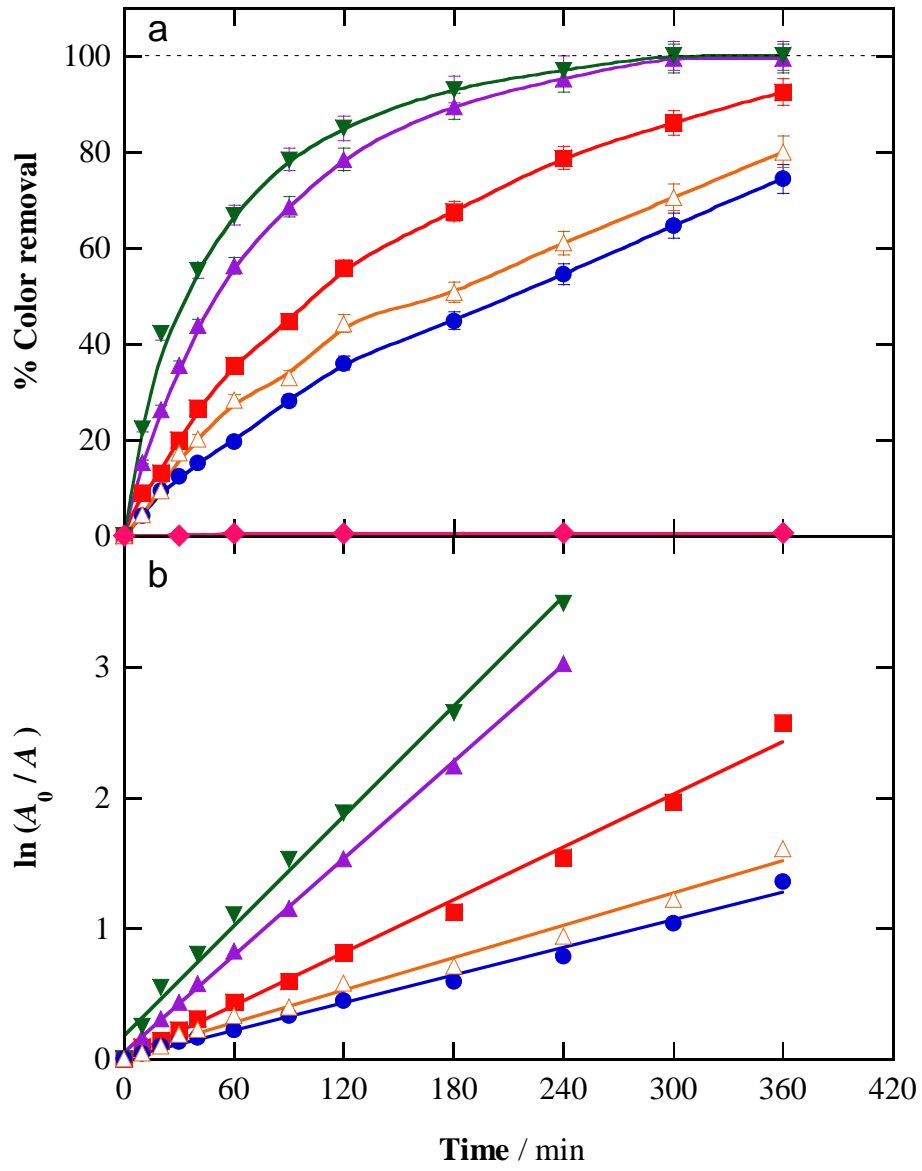


Fig. 1

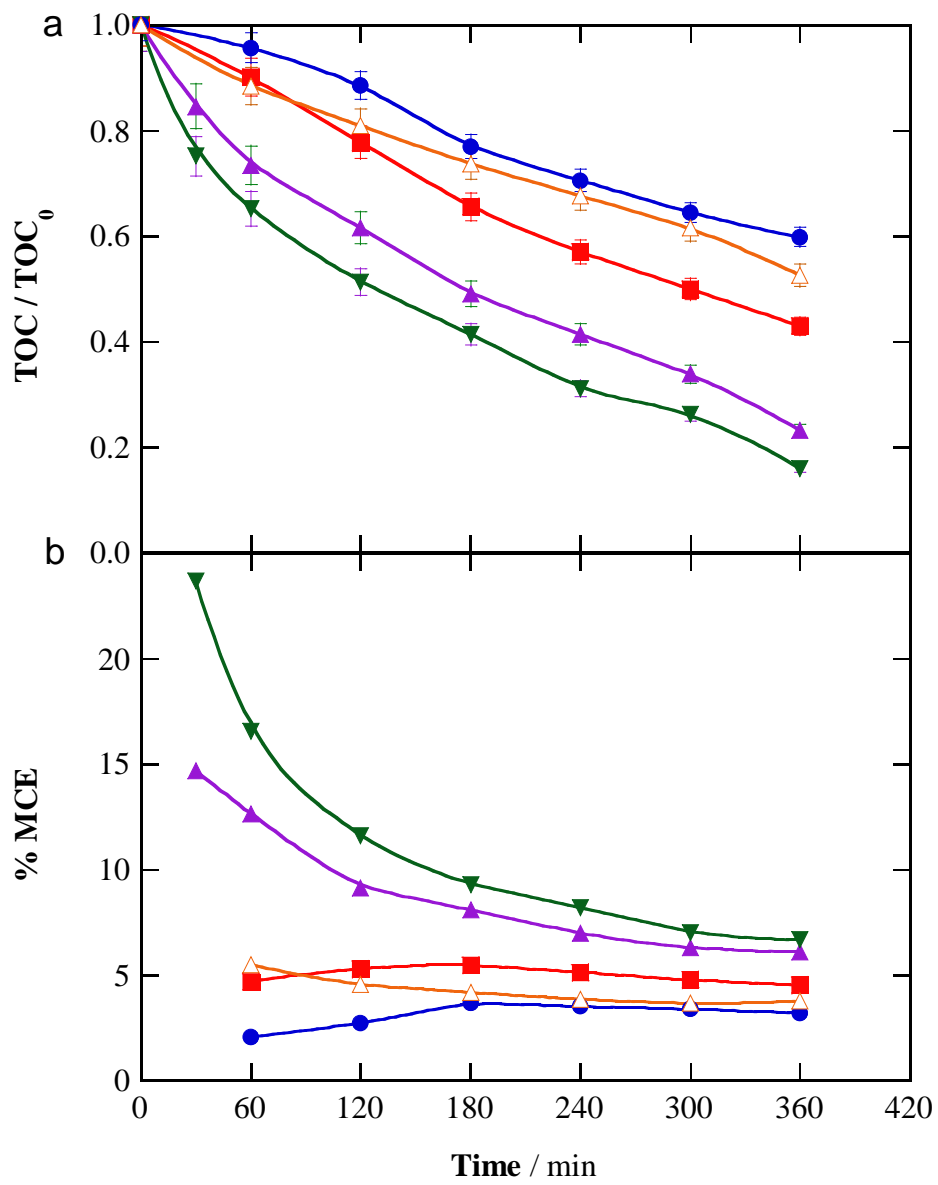


Fig. 2

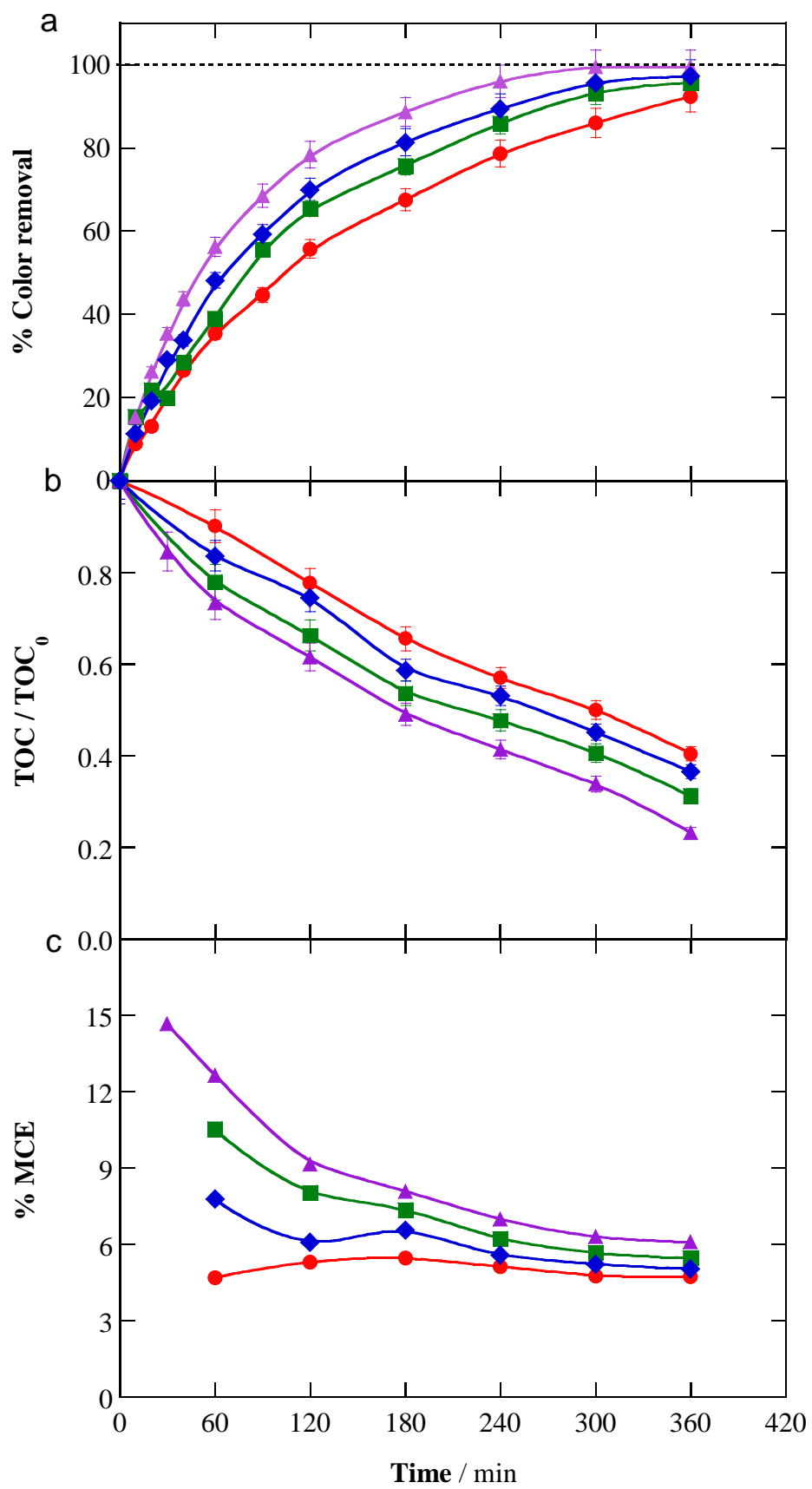


Fig. 3

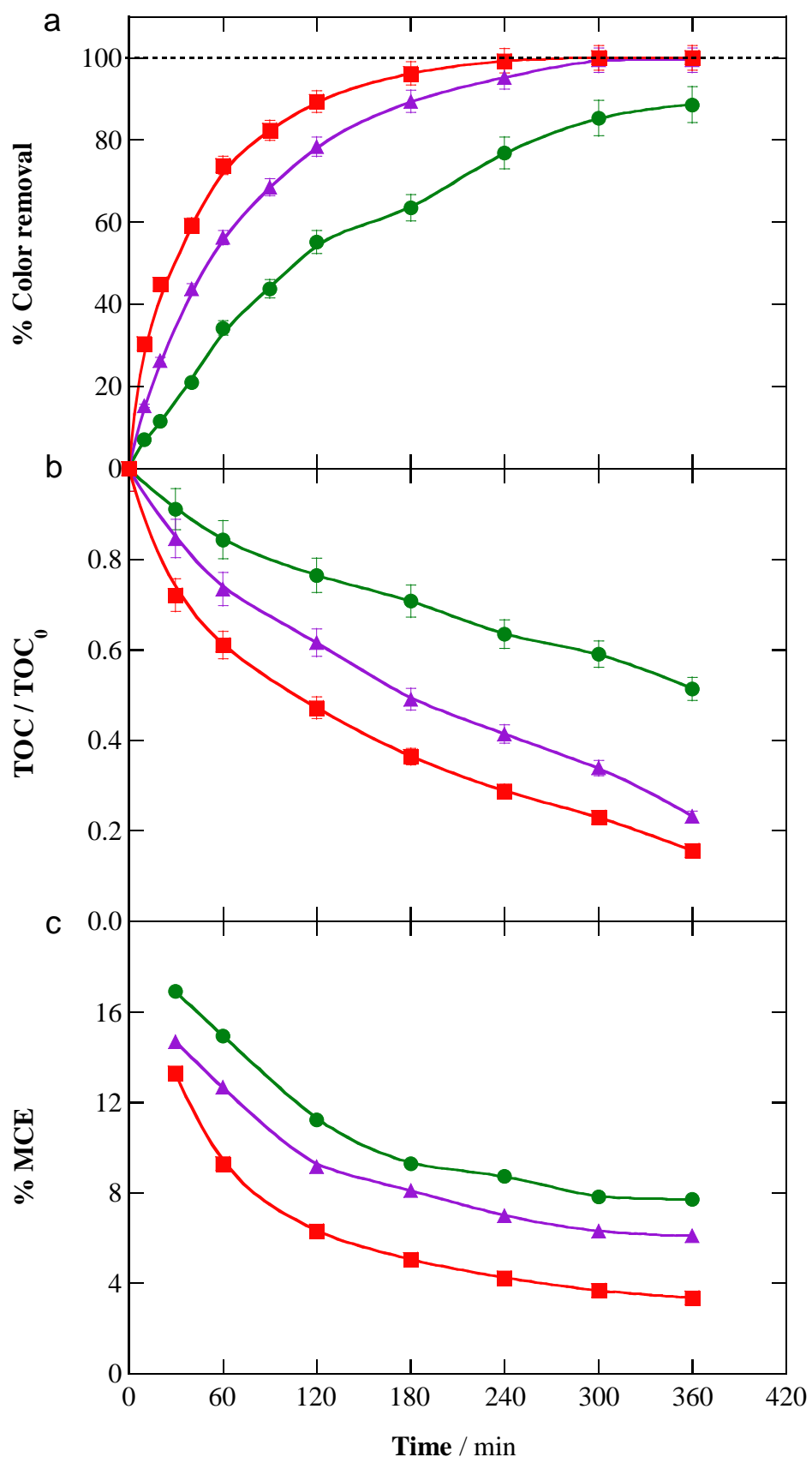


Fig. 4

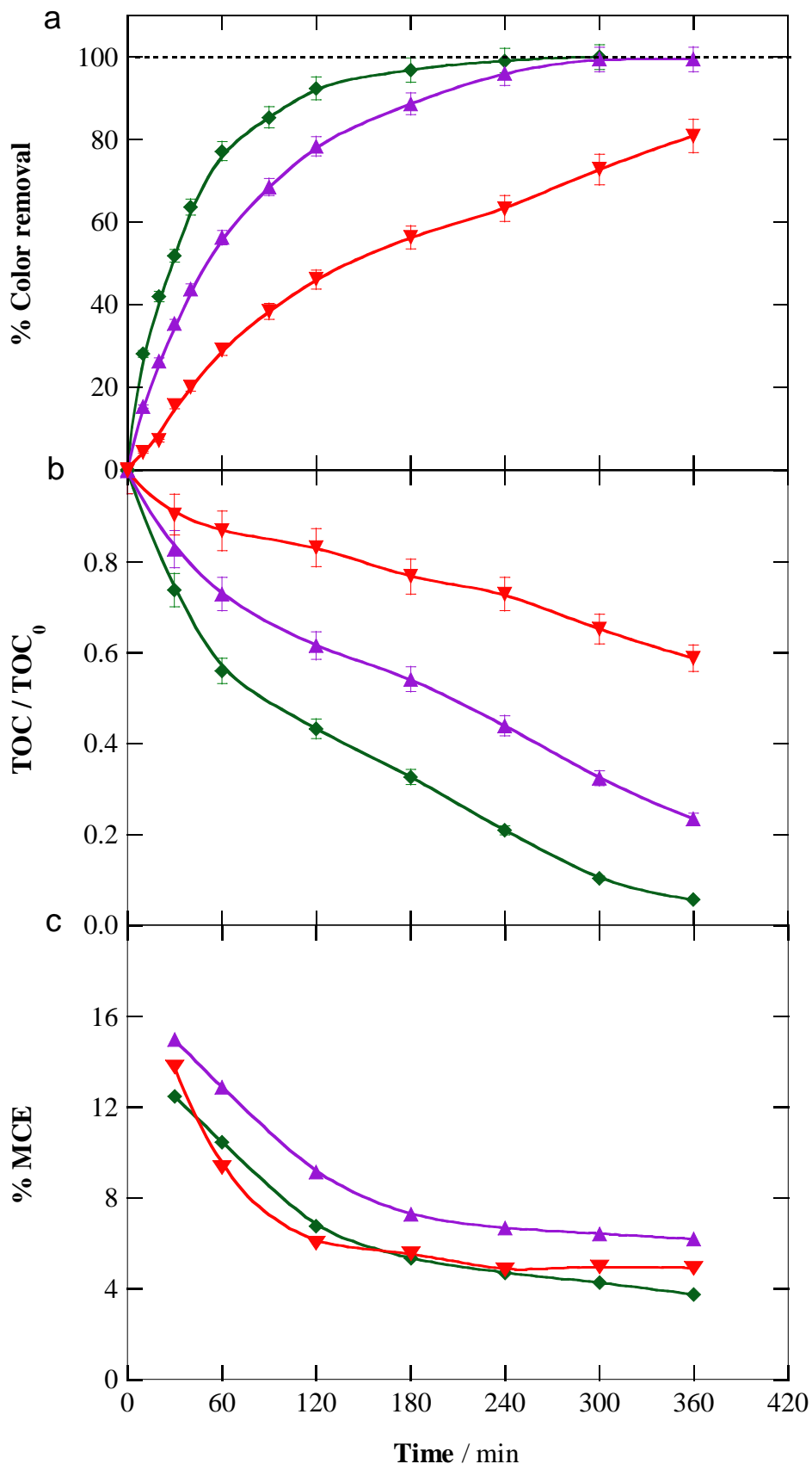


Fig. 5

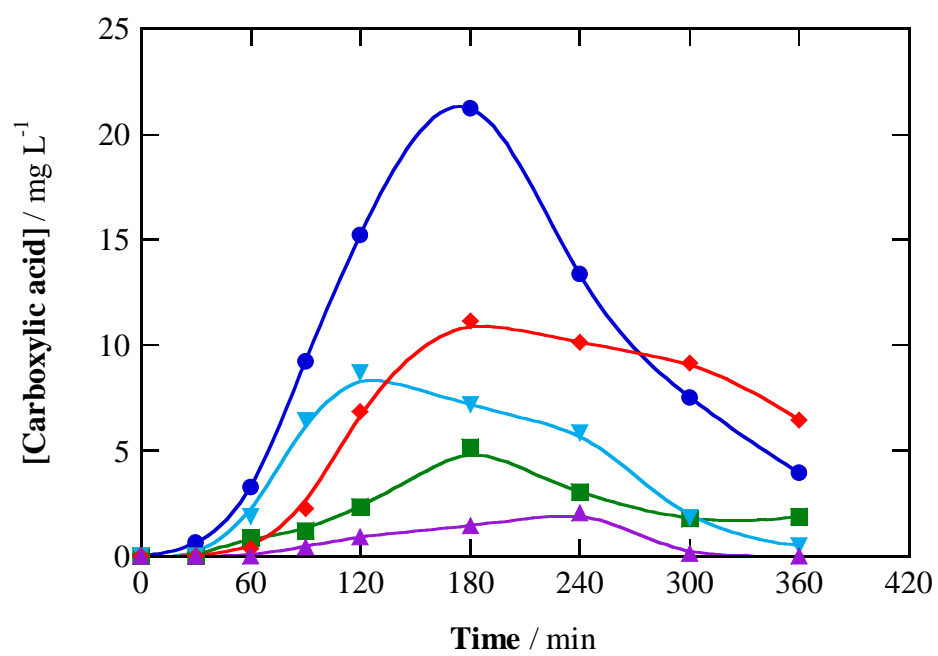


Fig. 6

Table 1.

Pseudo-first-order rate constant for decolorization, along with the square of the correlation coefficient, and percentage of TOC removal and mineralization current efficiency after 360 min of electrolysis of solutions containing 130 mL of Ponceau SS in 0.050 M Na₂SO₄ at pH 3.0 and 25 °C by different EAOPs using a BDD/air-diffusion electrode cell.

Method	[Ponceau SS] ₀ (mM)	[Sodium vermiculite] (g L ⁻¹)	<i>j</i> (mA cm ⁻²)	<i>k</i> _{dec} (min ⁻¹)	<i>R</i> ²	% TOC removal	% MCE	
AO-H ₂ O ₂	0.150	-	33.3	3.52×10 ⁻³	0.992	40.2	3.2	
EF with 0.018 mM Fe ²⁺	0.150	-	33.3	4.12×10 ⁻³	0.989	47.5	3.8	
EF-vermiculite	0.150	1.0	33.3	6.74×10 ⁻³	0.995	57.1	4.5	
PEF-vermiculite	0.075	1.0	33.3	2.09×10 ⁻²	0.993	94.4	3.7	
	0.150	0.25	33.3	6.70×10 ⁻³	0.994	59.7	4.7	
	0.150	0.50	33.3	8.58×10 ⁻³	0.995	68.9	5.4	
	0.150	1.0	16.6	6.08×10 ⁻³	0.996	48.7	7.7	
	0.150	1.0	33.3	1.23×10 ⁻²	0.998	76.9	6.1	
	0.150	1.0	66.6	1.74×10 ⁻²	0.993	84.5	3.3	
	0.150	2.0	33.3	9.87×10 ⁻³	0.996	63.5	5.0	
	0.225	1.0	33.3	4.37×10 ⁻³	0.992	41.3	4.9	
	SPEF-vermiculite	0.150	1.0	33.3	1.40×10 ⁻²	0.993	84.1	6.7